Magnetic phase diagram and multiferroicity of Ba₃MnNb₂O₉: A spin-$\frac{5}{2}$ triangular lattice antiferromagnet with weak easy-axis anisotropy

M. Lee,[1,2] E. S. Choi,[2,*] X. Huang,[3] J. Ma,[4] C. R. Dela Cruz,[4] M. Matsuda,[4] W. Tian,[4]
Z. L. Dun,[5] S. Dong,[3] and H. D. Zhou[5,2,†]

[1]*Department of Physics, Florida State University, Tallahassee, Florida 32306-3016, USA*
[2]*National High Magnetic Field Laboratory, Florida State University, Tallahassee, Florida 32310-3706, USA*
[3]*Department of Physics, Southeast University, Nanjing 211189, China*
[4]*Quantum Condensed Matter Division, Oak Ridge National Laboratory, Oak Ridge, Tennessee 37381, USA*
[5]*Department of Physics and Astronomy, University of Tennessee, Knoxville, Tennessee 37996-1200, USA*

We have performed magnetic, electric, thermal, and neutron powder diffraction (NPD) experiments as well as density functional theory (DFT) calculations on Ba₃MnNb₂O₉. All results suggest that Ba₃MnNb₂O₉ is a spin-5/2 triangular lattice antiferromagnet (TLAF) with weak easy-axis anisotropy. At zero field, we observed a narrow two-step transition at $T_{N1} = 3.4$ K and $T_{N2} = 3.0$ K. The neutron diffraction measurement and the DFT calculation indicate a 120° spin structure in the *ab* plane with out-of-plane canting at low temperatures. With increasing magnetic field, the 120° spin structure evolves into up-up-down (*uud*) and oblique phases showing successive magnetic phase transitions, which fits well to the theoretical prediction for the 2D Heisenberg TLAF with classical spins. Multiferroicity is observed when the spins are not collinear but suppressed in the *uud* and oblique phases.

I. INTRODUCTION

One simple example of the geometrically frustrated system is the two-dimensional (2D) triangular lattice antiferromagnets (TLAFs) [1–4]. At zero magnetic field, the ground state of TLAF is known to have a highly degenerate spin structure with three spins oriented 120° relative to each other. With increasing magnetic field, the magnetization process exhibits successive magnetic phase transitions. First, the spin structure yields to the so-called *Y* phase, where the spins tilted toward the external magnetic field deviating from the 120° ordered phase. Above a certain field, the up-up-down (*uud*) phase emerges, in which the magnetization is 1/3 of the saturation magnetization M_{sat} in a finite range of the external magnetic field, hence showing a magnetization plateau. For the classical spin systems such as with $S = 5/2$, the thermal fluctuations are known to stabilize the *uud* phase by a mechanism called order-by-disorder [5]. The existence of the *uud* phase in the finite range of temperature implies that the thermal fluctuations lift the degeneracy of the ground state. Without the thermal fluctuations, the *uud* phase would have been stabilized at a single point. In the order-by-disorder mechanism, the fluctuations lower the free energy of the system by selecting the highest entropic state, in which two spins align parallel with the external field direction and the other spin points in the opposite direction. At higher fields, the oblique phase, a canted version of the *uud* phase, is stabilized. Experimentally, RbFe(MoO₄)₂ (Fe³⁺, $S = 5/2$) [6,7] and Rb₄Mn(MoO₄)₃ (Mn²⁺, $S = 5/2$) [8] are typical examples of TLAFs with spin-5/2 that demonstrate the existence of the magnetic plateau at 1/3 M_{sat}.

More recently, multiferroicity, where magnetic orders are strongly correlated to the spontaneous electric polarization, has been reported in a few TLAFs. For example, RbFe(MoO₄)₂ [9–11] and ACrO2 ($S = 3/2$, $A =$ Ag and Cu) [12,13] have shown multiferroicity in the 120° and the *Y* phases where the spin chirality is nonzero for a triangular plaquette. In Ba₃NiNb₂O₉ ($S = 1$) [14] and Ba₃CoNb₂O₉ ($S = 1/2$) [15], the multiferroicity was observed not only in the noncollinear spin state but also in the *uud* and oblique phases. So far, considerable efforts have been made to understand the multiferroicity of various magnetic materials [16–21]. The exchange striction [22–24], the spin current model [25], and the inverse DM mechanism [26] have been successfully used to explain the multiferroicity in some types of materials. Nevertheless, a unified picture for magnetic-controlled ferroelectric materials is still not complete especially for multiferroic TLAFs. Part of the reason is that there are not many TLAFs showing multiferroicity with variations of structures and magnitude of spins and so forth. Considering the few known cases of multiferroic TLAFs, the spin chirality seems to be a key factor for the multiferroicity in TLAFs with large spins while not so much in TLAFs with small spins.

In this paper, we studied another TLAF with spin-5/2, Ba₃MnNb₂O₉, with experimental and theoretical probes and constructed a phase diagram. Various experimental techniques such as dc and ac susceptibility, magnetization, specific heat, neutron powder diffraction (NPD), dielectric constant, and electric polarization were employed, and density functional theory (DFT) calculations were performed. The results suggest that Ba₃MnNb₂O₉ makes a very good example of quasi-2D Heisenberg TLAF with weak easy-axis anisotropy. We also found that Ba₃MnNb₂O₉ is multiferroic in the 120° and the *Y* phases but not in the collinear spin phases, which are different from its sister compounds Ba₃NiNb₂O₉ and Ba₃CoNb₂O₉.

———————
*echoi@magnet.fsu.edu
†hzhou10@utk.edu

II. EXPERIMENTAL

Polycrystalline-Ba$_3$MnNb$_2$O$_9$ samples were prepared using solid state reaction method. Stoichiometric mixtures of BaCO$_3$, MnO, and Nb$_2$O$_5$ were ground together and calcined in Ar gas at 1230 °C for 24 hours. The room temperature powder x-ray diffraction (XRD) shows that the equilateral triangular lattice layers are formed by magnetic ions of Mn, and each layer is separated by two nonmagnetic Nb layers in Ba$_3$MnNb$_2$O$_9$, with the space group *P*-3*m*1 and lattice parameters $a = b = 5.7737$ Å and $c = 7.0852$ Å. This is isostructural with the previous reported TLAFs, Ba$_3$NiNb$_2$O$_9$ [14] and Ba$_3$CoNb$_2$O$_9$ [15].

The dc magnetization was measured using a vibrating sample magnetometer (VSM) at the National High Magnetic Field Laboratory and a commercial SQUID magnetometer (MPMS, Quantum Design). The VSM was calibrated with a standard Ni sphere. The ac susceptibility data were obtained with a homemade ac susceptometer.

The neutron powder diffraction (NPD) measurements down to 1.5 K were performed using the HB2A powder diffractometer at the High Flux Isotope Reactor (HFIR), Oak Ridge National Laboratory (ORNL). About 3 g of powder was loaded in a vanadium can with an inner diameter of 12 mm. The diffraction data were collected using the wavelength $\lambda = 2.406$ Å and collimation of 12′-open-6′, which would provide a better Q resolution at low Q for investigating magnetic structures. Additional measurements down to 0.3 K were carried out on the HB1A triple-axis spectrometer at HFIR employing a ^{3}He insert system. HB1A was operated with a fixed incident neutron energy of 14.6 meV using a double pyrolytic graphite (PG) monochromator system and PG analyzer. A collimation of 40′-40′-40′-80′ was used and contamination from higher-order beams was removed using two PG filters placed after each monochromator. The diffraction data were analyzed using the Rietveld refinement program FullProf [27].

For the dielectric constant and electric polarization measurements, a polycrystalline sample was polished into a plate shape with typical dimensions of $4 \times 4 \times 0.1$ mm^3 to have a parallel capacitor geometry. The electrical contacts were made by silver epoxy on the two flat surfaces. The capacitance of the sample was measured with an Andeen-Hagerling AH-2700A commercial capacitance bridge, and the dielectric constant was obtained by approximating the sample as an infinite parallel capacitor. The electric polarization was obtained by integrating the pyroelectric current signal (I_p) in the time domain. For I_p measurement, the sample was cooled in the presence of electric field (poling) and/or magnetic field. The detailed procedure of I_p measurement has been published elsewhere [15].

III. RESULTS

A. dc magnetic susceptibility and specific heat

We show the temperature dependence of the dc magnetic susceptibility ($\chi = M/H$) measured at various fields in Fig. 1. The inset of Fig. 1 shows the inverse susceptibility ($1/\chi$) for $\mu_0 H = 1$ T, which is linear in T following the Curie-Weiss law at high temperatures. At low temperatures, χ (T) shows features of magnetic transitions; for example, the 0.1 T data
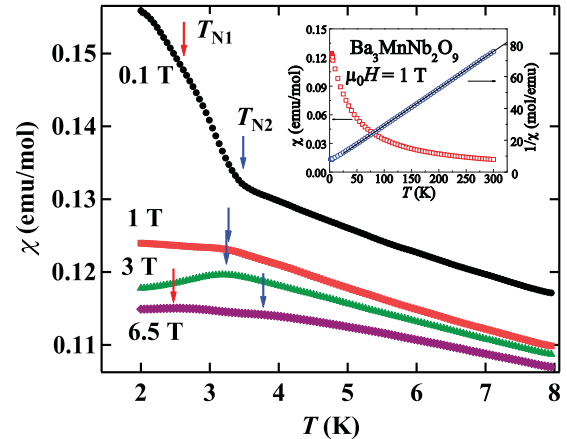

FIG. 1. (Color online) Temperature dependence of the dc magnetic susceptibility obtained at various fields. Inset : the susceptibility at 1 T and its inverse. The symbols are experimental data, and the black solid line is the linear fitting using the Curie-Weiss law.

show an upturn (denoted as T_{N1}) and a shoulderlike structure at a lower temperature (denoted as T_{N2}). At higher fields, there is only a broad peak visible for $\mu_0 H = 1$ and 3 T data, while two broad peaks appear for 6.5 T data. Relying on the features observed from the raw data (the first derivative $d\chi/dT$ did not give us consistent phase transition features), we assigned T_{N1} as the temperature of the upturn or the high-T peak and T_{N2} as low-T peak. T_{N1} is about 3.5 K at $\mu_0 H = 0.1$ T and increases to 3.8 K at 6.5 T.

Using the Curie-Weiss law, we obtained $\mu_{eff} = 5.86\,\mu_B$ and $\Theta_{CW} = -26$ K from the T dependence at high temperatures. The μ_{eff} agrees well with the theoretical value 5.93 μ_B with an assumption of spin-only $S = 5/2$ contribution [28]. The negative Weiss constant suggests the transitions at lower temperatures are originated from paramagnetic (PM) to antiferromagnetic ordering. According to the mean field theory, θ_{CW} is given as $(-zJS(S+1))/3$ k$_B$, where J is the exchange interaction of the Heisenberg Hamiltonian, $J\sum_{\langle i,j\rangle} S_i \cdot S_j$, and z is the number of nearest neighbors. For the $S = 5/2$ triangular lattice with $z = 6$, we obtained $J/k_B = -2/3\theta_{CW} = 1.45$ K from the χ (T) result.

The specific heat data taken at different fields are shown in Fig. 2. At zero field, two clear peaks are observed at 3.29 and 3.04 K, which survives up to 2 T. At higher fields, only a single peak becomes visible at the measured temperature range. The positions of the first high-T peak at $\mu_0 H = 0$ and 1 T are very similar to T_{N1}'s from the χ measurement indicating a long range magnetic ordering at T_{N1}. The low-T peak denoted as T_{N2} is also close to T_{N2} from the $\chi(T, \mu_{0H} = 0.1$ T) data indicating another long range ordering. As the magnetic field increased, T_{N1} increases initially up to $\mu_{0H} = 6$ T and decreased with further increasing field, while T_{N2} decreases only slightly.

B. Neutron powder diffraction

We performed neutron powder diffraction (NPD) experiments to identify the spin structure at zero field. The pattern measured at 1.5 K was shown in Fig. 3(a). According to
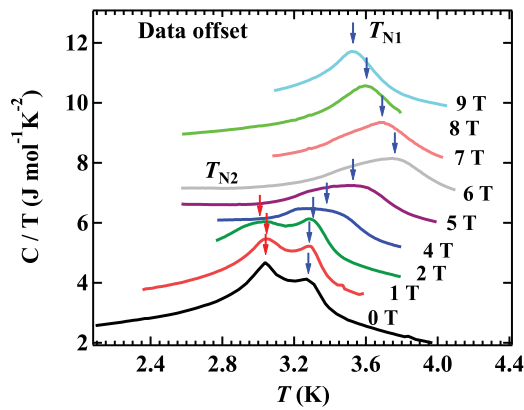
FIG. 2. (Color online) Specific heat divided by temperature as a function of temperature for magnetic fields up to 9 T. At 0, 1, and 2 T, two clear peaks are observed marked as T_{N1} and T_{N2}. As the field increases, a single peak at T_{N1} was observed. Data offset by 1 J mol^{-1}K^{-2} gradually from the 0 T data.

the refinement, the magnetic Bragg peaks are observed at $Q = (n_1 + 1/3, n_2 + 1/3, n_3)$ (n_i: integer). In Fig. 3(e), the difference between the 5 and 1.5 K patterns clearly shows the details of these magnetic Bragg peaks. The refined magnetic structure and the crystal structure of Ba$_3$MnNb$_2$O$_9$ are shown in Figs. 3(b), 3(c), and 3(d). It is a 120° antiferromagnetic

ordering in the *ab* plane with out-of-plane cantings. The canting angles are $\varphi = 8.7(4)°$ and $\psi = 18.7(9)°$, respectively. In addition, it is collinear ferromagnetic spins between the nearest neighbor layers. The refined ordered moment is 4.71(25) μ_B for each Mn^{2+} ion. Figure 3(f) shows the order parameter of (1/3, 1/3, 0) between 0.3 and 5 K. Only one magnetic transition was clearly identified at T_N around 3.3 K within the resolution limit of our experiment. The structural and magnetic parameters obtained by refining the 1.5 K data are listed in Table I. The refinement results of the 0.3 K data (not shown here) do not show significant difference from that obtained at 1.5 K within the resolution limit.

C. dc magnetization and ac susceptibility

Figure 4 shows the field dependence of the dc magnetization $M(H)$ and its derivative dM/dH at 1.5 K. Above 30 T, $M(H)$ increases slowly due to the polycrystallinity of the sample before the saturation with $M_{sat} \sim 4.9$ μ_B. The saturation value and the overall shape of the magnetization is similar to reported values [29]. $M(H)$ shows weak but notable inflections around 5.5, 9.3, and 12.4 T, which are more clearly seen from dM/dH as a peak-valley-peak structure. The magnetization value at the valley is $\sim 1.7\mu_B$, close to 1/3 M_{sat}. The shape of dM/dH is reminiscent of what was observed in other TLAF single crystal [6,8,30] or polycrystal [31] samples reported to have a magnetization plateau. Although the $M(H)$ curve
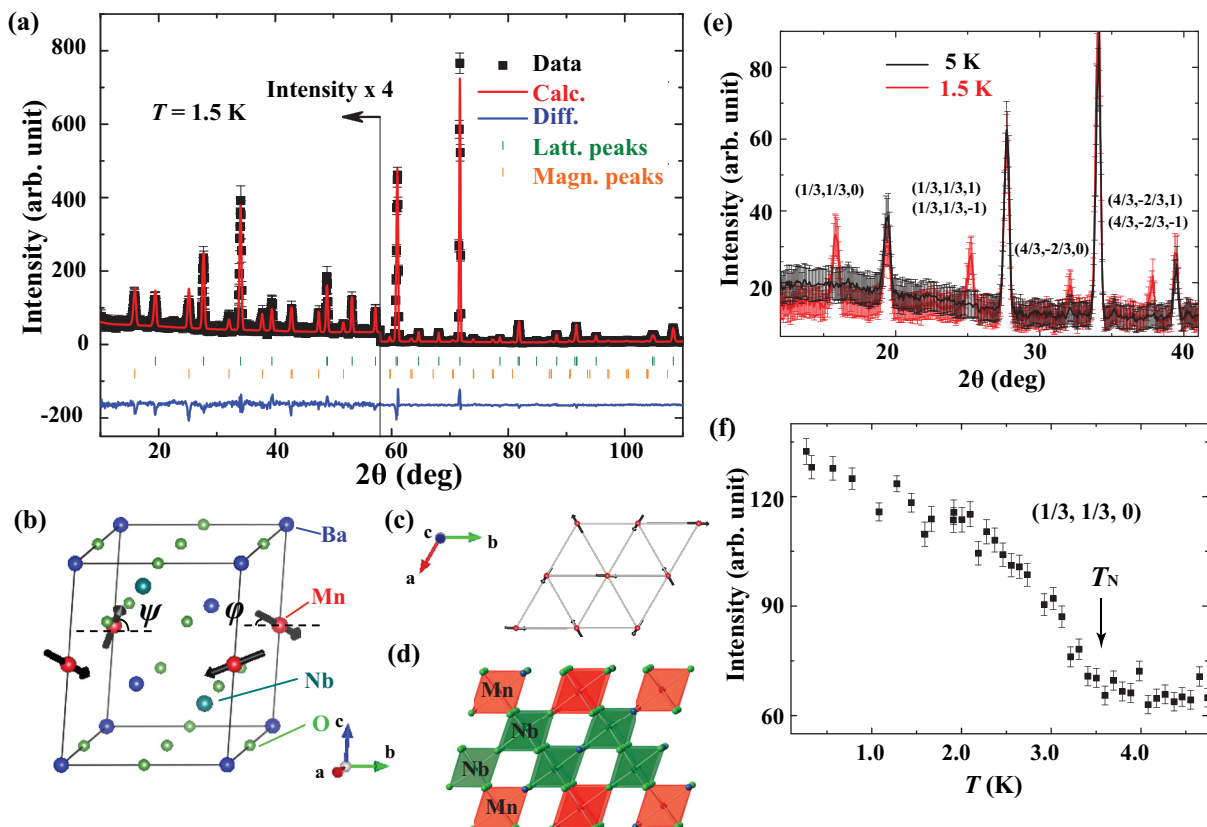

FIG. 3. (Color online) (a) The neutron powder diffraction (NPD) pattern obtained at 1.5 K. The red solid curve is the best fit from the Rietveld refinement by using FULLPROF. (b) Triangular lattice composed of Mn^{2+} ions and its spin structure at zero field. (c) Unit cell of Ba$_3$MnNb$_2$O$_9$ and spin structure of Mn ions. (d) Crystal structure for Ba$_3$MnNb$_2$O$_9$: the red octahedra represent Mn sites and the green octahedra represent Nb sites. (e) NPD patterns taken at 1.5 and 5 K. (f) Order parameter of (1/3, 1/3, 0) between 0.3 and 5 K.

TABLE I. Structural and magnetic parameters obtained by the Rietveld refinement for the NPD pattern at $T = 1.5$ K.

Atom	x	y	z
Ba(1)	0.3333	0.6667	0.6617(13)
Ba(2)	0.0000	0.0000	0.0000
Mn	0.0000	0.0000	0.5000
Nb	0.3333	0.6667	0.1762(10)
O(1)	0.5000	0.0000	0.0000
O(2)	0.1726(7)	0.3452(13)	0.3229(8)
Space group	Lattice parameters (Å)	RF-factor	Bragg R-factor
P-$3m1$	$a = 5.8036(1)$, $b = 5.8036(1)$, $c = 7.0808(3)$	5.84	6.91
	$\alpha = \beta = 90°, \gamma = 120°$		
Magnetic space group	Momentum		
P-1	4.91(25) μ_B		

here is not as apparent as in those compounds, dM/dH and the 1/3 M_{sat} magnetization value imply the magnetization plateau in the *uud* phase. Accordingly, we assigned the peak fields as $\mu_0 H_{c1}$ and $\mu_0 H_{c2}$ as phase boundaries of Y-*uud* and *uud*-oblique phase, respectively. At higher fields, dM/dH decreases rapidly above $\mu_0 H_{c3}$, above which spins enter polarized states due to the external magnetic field. The polycrystallinity of the sample and the easy-axis anisotropy (to be discussed later) are probably the reasons why the magnetization plateau was not clearly observed.

To further study magnetic phase transitions at lower temperatures and at different fields in more detail, ac magnetic susceptibility (χ') measurements were performed. In Fig. 5(a), we show the temperature dependence of the ac magnetic susceptibility $\chi'(T)$ at 1 and 0.4 T. The overall temperature dependence of χ' measured at 1 T is similar to dc susceptibility $\chi(T)$ data at the same field, which is expected because $\chi'(T)$ usually resembles χ for nonglassy systems (as is the case in our work). We therefore assigned the prominent peak temperature of χ' as T_{N1} (slightly larger than the value obtained from the χ measurement), which is likely from a transition from PM to an ordered state. At lower temperatures below 1 K, there is another shoulderlike feature whose temperature is assigned as T_{N3}, which becomes more prominent for 0.4 T data.

At lower fields, we observed even more features, whose temperatures are assigned as T_{N1}, T_{N2}, and T_{N3} as shown in Fig. 5(b). We note T_{N2} at zero field is close to the lower T peak

of the zero field specific heat data (T_{N2} in Fig. 2) and also to the lower T feature of the $\chi(T)$ at 0.1 T (T_{N2} in Fig. 1), consistent with a long-range magnetic phase transition at T_{N2}. Upon cooling, $\chi'(T)$ initially increases rapidly (instead of peak at higher fields) at T_{N1}, followed by a shoulder at T_{N2} and a peak at T_{N2}. Both theoretical and experimental works have shown that the temperature dependence of magnetic susceptibility can probe phase transitions from PM-*uud*-Y phase in TLAF [8,32,33]. The detailed temperature dependence of χ' at different fields is not completely understood yet, but some of the features are similar to what was predicted by the Monte Carlo (MC) simulation [32] or to the reported experimental work [8]. For example, according to a MC simulation result, the rapid increase of χ' at low fields at T_{N1} is a result of the ferrimagnetic ordering for the z-component (out-of-plane) moment while the xy-component (in-plane) remains paramagnetic.

At higher fields above 0.3 T, χ' shows a prominent peak at T_{N1}, which is also observed from Rb$_4$Mn(MoO$_4$)$_3$ [8] (note that the phase boundary in their work was defined differently as a peak of $d\chi/dT$). As the field is increased, the shoulder structure at T_{N2} also evolves into a more prominent peak [see Fig. 5(c)] until it becomes too low to be detected. At high
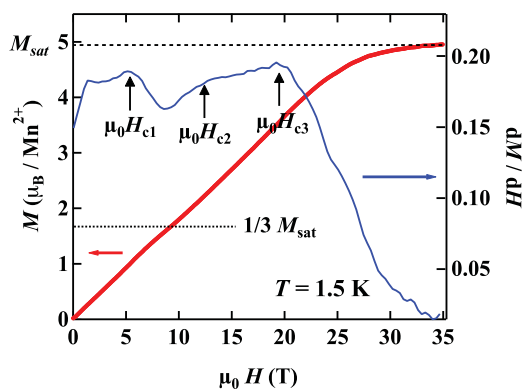

FIG. 4. (Color online) The high-field dc magnetization curve obtained at 1.5 K up to $\mu_0 H = 35$ T (red curve) and its first derivative (blue curve).
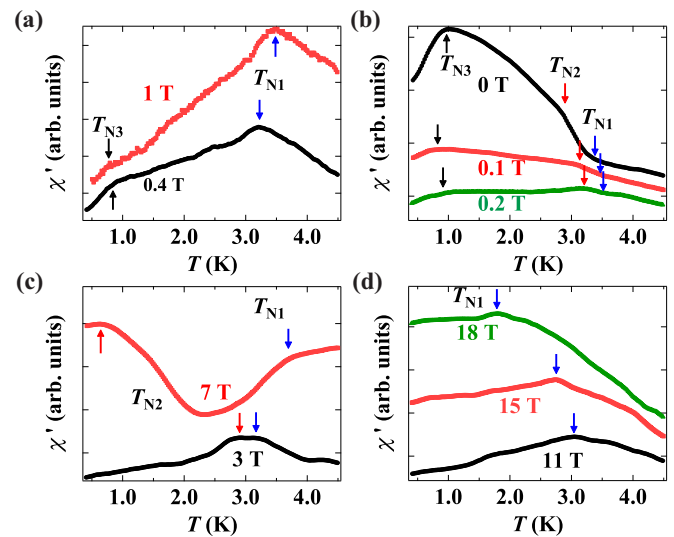

FIG. 5. (Color online) Temperature dependence of the ac magnetic susceptibility $\chi'(T)$ measured at different fields of (a) 0–0.2 T, (b) 0.3–1 T, (c) 3–7 T, and (d) 11–18 T. Data are offset.
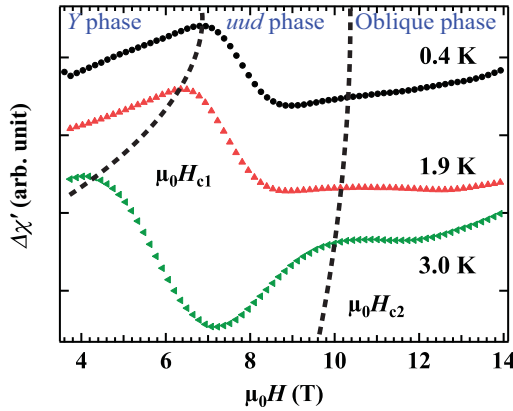
FIG. 6. (Color online) Field dependence of the ac magnetic susceptibility ($\chi'(H)$) measured at various temperatures. $\Delta\chi'(H,T) = \chi'(H,T)-\chi'(H,T = 5\ \mathrm{K})$ are shown. Three different phases divided by two dotted lines were assigned. Data are offset.

fields above 10 T, only T_{N1} was observed in the measured temperature range, as it decreases with increasing fields.

The field dependence of the ac susceptibility $\chi'(H)$ measured at three temperatures is shown in Fig. 6. $\chi'(H)$ is sensitive to magnetic phase transitions since it probes dM/dH directly. In Fig. 6, we plot $\Delta\chi'(H,T) = \chi'(H,T)-\chi'(H,T = 5\ \mathrm{K})$ to emphasize the field induced phase transitions. All three curves show a similar structure with increasing field; peak-valley-peak structure as seen from dM/dH obtained from the dc magnetization data. The width between the two peaks, the *uud* phase with magnetization plateau, becomes wider as the temperature increases, which implies that the thermal fluctuations play an important role to stabilize the order-by-disorder driven phase.

D. Dielectric constant and polarization

Figure 7 shows the temperature dependence of the dielectric constant ε' at different fields. At zero field, two features were observed: an abrupt increase of ε' around $T = 3.4$ K followed by a peak around $T = 3.0$ K, whose temperatures are again similar to those from $\chi(T)$, $\chi'(T)$, $C_p(T)$. Therefore we assigned them as T_{N1} and T_{N2} accordingly. With increasing fields, the two features evolve differently; T_{N2} shifts rapidly to lower temperatures and the peak becomes broader, while T_{N1} increases with fields up to 7 T before starts to decrease at higher fields. There is a shoulderlike anomaly denoted as an asterisk for the data taken between $\mu_0 H = 4$ and 8 T, which was not observed from other experimental techniques.

The field dependence of the dielectric constant is shown in Fig. 8. As the field is increased from zero field, a first prominent peak is apparent at each temperature, whose position increases with decreasing temperature. The position and its temperature dependence is similar to those of $\mu_0 H_{c1}$ obtained from the $\chi(H)$ and the $M(H)$ measurements. There are also features related to critical fields, $\mu_0 H_{c2}$ and $\mu_0 H_{c3}$, seen as a much broader peak and a slope change (see the inset of Fig. 8). At lower temperatures, all the features related to the critical fields become weaker implying the importance of thermal fluctuations, and $\mu_0 H_{c2}$ and $\mu_0 H_{c3}$ become too weak to be identified from the $\varepsilon'(H)$ data.
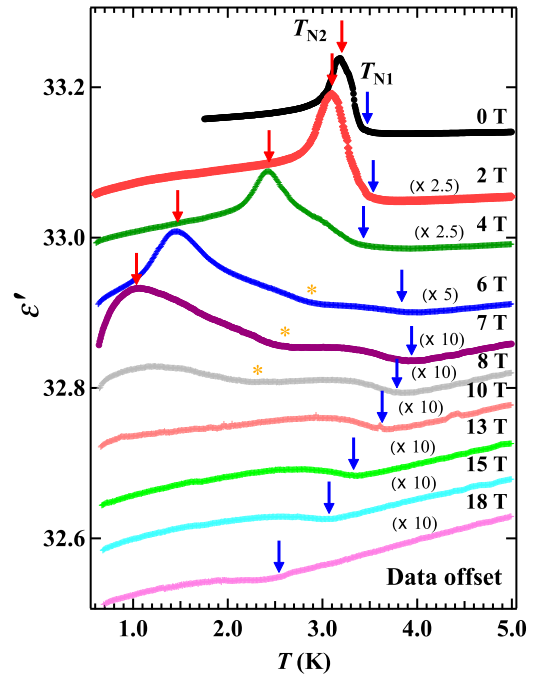

FIG. 7. (Color online) Temperature dependence of the dielectric constant ($\varepsilon'(T)$) at different magnetic fields. Data are scaled as indicated and offset from the 0 T data. The raw data have similar values, for example, 33.136 at 0 T and 33.139 at 18 T at 5 K.

The sharp peaks at T_{N2} in dielectric constants imply the changes of electric properties. The electric polarization (P) was obtained via the pyroelectric current (I_p) measurement to investigate a possibility of ferroelectricity. Figure 9(a) shows
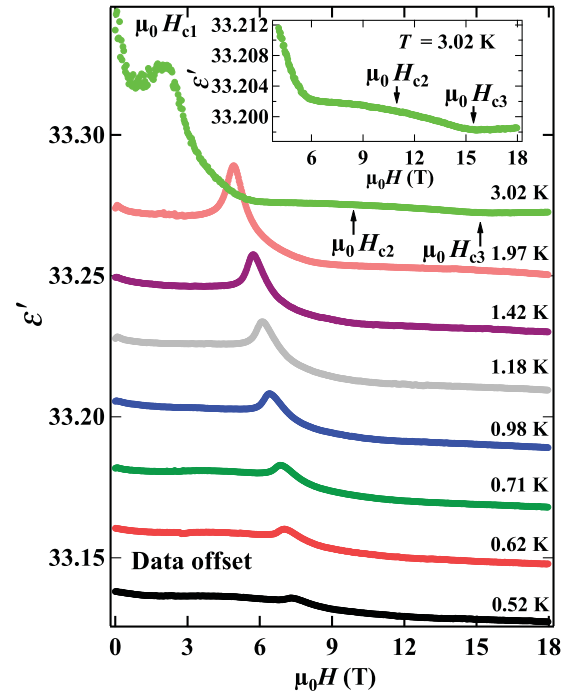

FIG. 8. (Color online) Field dependence of the dielectric constant ($\varepsilon'(H)$) at different temperatures. Data are offset by 0.02 from 0.52 K data.
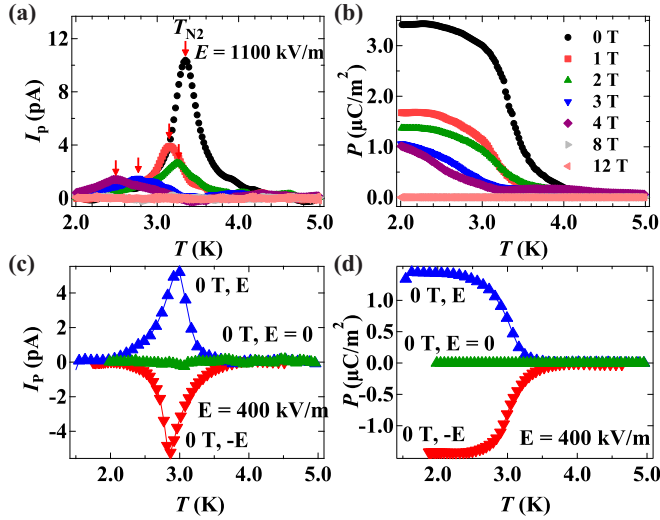
FIG. 9. (Color online) Temperature dependencies of (a) pyro-electric current and (b) polarization measured with $E = 1100$ kV/m at different fields. (c) and (d) show the pyroelectric current and polarization measured under different conditions of electric field poling.
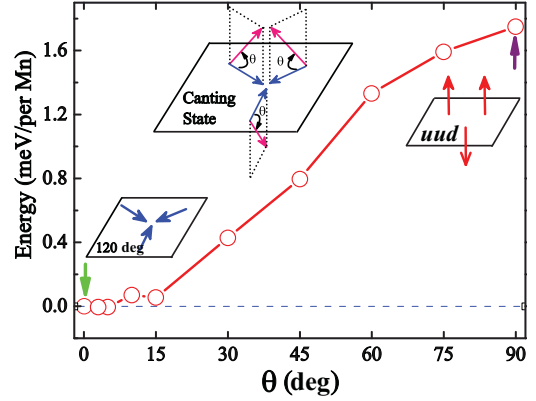

FIG. 10. (Color online) Density functional theory (DFT) energy as a function of tilting spin angle, rotating from the in-plane 120° structure to the complete out-of-plane *uud* structure. The energy of 120° structure is the reference point. θ is defined as the angle between spins and the *ab*-plane. Two of the three spins tilt up, while the last one tilts down.

I_p measured at different fields from 0 to 12 T and the resulting P is shown in Fig. 9(b). The I_p shows a peak at similar temperatures to T_{N2}. With increasing field, it shifts to lower temperatures while becoming weaker and broader. The I_p completely disappears above 5 T in the measured temperature range. Accordingly, the P shows the maximum of polarization of 3.45 μC/m^2 at zero field and decreases with increasing field and eventually suppressed above 5 T. We note here that there is no feature of I_p at the phase boundary of either PM-*uud* or PM-oblique phases at all measured fields, therefore no polarization in the *uud* and the oblique phase. As seen from Figs. 9(c) and 9(d), I_p and P were observed only in the presence of the electric field poling. and the directions of I_p and P can be reversed poling in the opposite direction. We also found that the presence or absence of magnetic field during cooling didn't make any difference. The spontaneous and reversible polarization confirms the ferroelectricity concomitant with the magnetic phase transition, hence multiferroelectricity.

E. DFT calculation

To help the understanding of experimental observations, a density functional theory (DFT) calculation was performed using the Vienna *ab initio* simulation package (VASP) [34,35]. An in-plane enlarged supercell consisting of three chemical units of Ba$_3$MnNb$_2$O$_9$ with experimental structures was used in the following calculations [36]. The projector augmented wave (PAW) potentials were adopted [37,38], the plane-wave cutoff energy was 500 eV, and a $5 \times 5 \times 6$ Monkhorst-Pack k-point mesh centered at the Γ point was used. The electronic correlation was treated using the generalized gradient approximation (GGA) plus Hubbard U [39,40]. The effective Hubbard parameter $U_{eff} = U - J = 3$ eV was applied to the $3d$ electrons of Mn ion. To account for noncollinear spin orders, the spin-orbit coupling is enabled in all following calculations.

The magnetic ground phase is checked by comparing the energies of various magnetic patterns. In our DFT calculation, the in-plane 120° structure is lower than the out-of-plane *uud* one for ~1.7 meV/per Mn. Within the Wigner-Seitz sphere defined in the PAW potential, the local magnetic moment of Mn is about 4.4 μ_B in both these two phases, implying the high-spin state, in agreement with the experimental observation.

Furthermore, to test the canting ground state observed in the above neutron study, the spin directions of Mn's are rotated from the in-plane 120° structure to the out-of-plane *uud*, characterized by a tilting angle from the original spin plane. The energy difference is shown in Fig. 10 as a function of tilting angle. The global tendency is that the energy difference increases with the tilting angle. However, in a small tilting angle range (e.g. <5°), the energy is almost degenerate
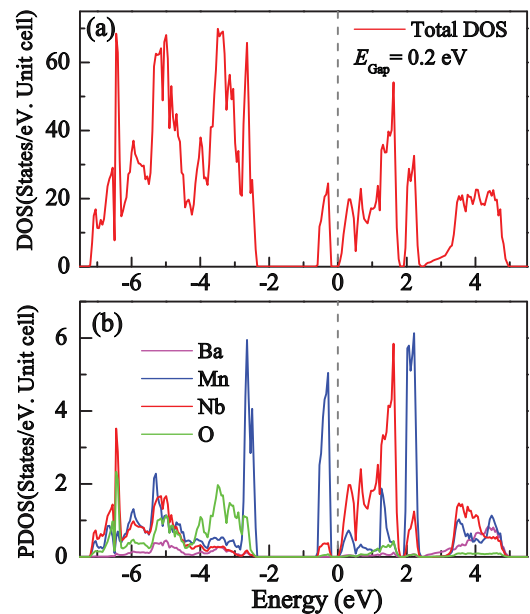

FIG. 11. (Color online) Density of states (DOS) of the 120° structure. (a) Total DOS. (b) Atomic-resolved DOS.

with the 120° structure one. The energy fluctuation in this region is beyond our DFT precision. Hence, according to our calculation, the ground state is the in-plane 120° structure, with or without a small out-of-plane tilting angle. Such a theoretical result agrees with the experimental observation qualitatively.

According to the density of states (DOS), the 120° structure state is insulating, with a small band gap of 0.2 eV, as shown in Fig. 11(a). The atomic-projected DOS (PDOS) [Fig. 11(b)] shows that the topmost valence bands are mostly from Mn's $3d$ orbitals (the e_g doublets), while the lowest conducting bands are from Nb's $4d$ orbitals (the t_{2g} triplets), in agreement with the expected valences: Mn^{2+} and Nb^{5+}. Therefore, here Nb ions are not directly involved in the magnetism.

IV. DISCUSSION

A magnetic field versus low temperature phase diagram was constructed by combining the data from Sec. III as shown in Fig. 12. Some phase boundaries are not apparent throughout the various experimental techniques and there are uncertainties (large error bars) in determining the phase boundaries. For example, the dielectric constant anomalies denoted as asterisks in Fig. 7 and the low temperature anomaly observed from the $\chi'(T)$ (denoted as T_{N3} in Fig. 5) are not detected by other experimental techniques. Nevertheless, there are clear patterns in the phase diagram when all the possible phase transition points are plotted in a single graph. We discuss our results below based on the common patterns while keeping in mind the existing theories and our DFT calculation result.

We observed three magnetic phases in addition to the paramagnetic phase. The three phases are well known: the Y phase, the uud phase with $1/3$ M_{sat} plateau, and the oblique phase [6–8,41]. First, we note the existence of the two-step transition; i.e., uud phase between PM and 120° (or Y phase). Theoretically, the two-step magnetic transition was predicted for TLAFs with easy-axis anisotropy, while a direct, single-step transition for TLAFs with easy-plane anisotropy. The easy axis anisotropy is also consistent with the NPD result,
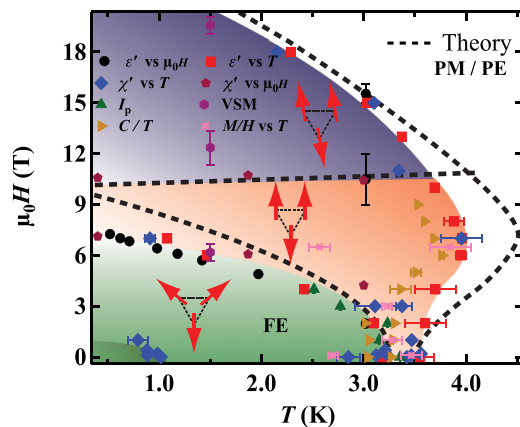

FIG. 12. (Color online) Magnetic field versus low temperature phase diagram. Different symbols represent phase transitions obtained from different experimental techniques, and the shaded regions with different colors are guide to the eyes. Error bars are drawn for the points with large uncertainties. The dotted line is the theoretically predicted phase diagram for a Heisenberg TLAF with $D/J \sim 0$.

which showed a 120° spin structure with out-of-plane canting at zero field. The DFT calculation also predicted a possible out-of-plane canting of the 120° spins with smaller canting angle (less than 5°) than the NPD result.

The magnetic phase transitions at zero field can be described as following. When the temperature is lowered above from the PM state, the easy-axis anisotropy first breaks a discrete C_3 symmetry of the lattice, and the system first enters into a long-range ordered uud phase between T_{N2} and T_{N1}. Upon further cooling below T_{N2}, the system exhibits canted Y state. The phase diagram is similar to another S-5/2 TLAF, $Rb_4Mn(MoO_4)_3$, which also exhibits easy-axis anisotropy [8]. We can estimate the single-ion anisotropy energy D from the two-step transition temperatures as $D \sim J(T_{N1}\text{-}T_{N2})/T_{N1}$ [42]. We obtained $D = 0.06\,J$, a much smaller value compared to that of $Rb_4Mn(MoO_4)_3$ ($D = 0.22\,J$) [8]. On the other hand, it is reported that isotropic or easy-plane anisotropy systems do not show uud phase at $H = 0$ [6,7,43].

The experimental phase diagram of $Ba_3MnNb_2O_9$ is very similar to the theoretical phase diagram of a classical Heisenberg TLAF obtained by a MC simulation [33]. When we scaled the MC simulated phase diagram using $J = 1.4$ K (the value obtained from the Curie-Weiss fitting) to the experimental phase diagram, it is clear both phase diagrams agree well each other qualitatively and quantitatively. One deviation is found that the observed uud phase does not extend as much as the theoretical prediction. It is possible that the deviation is originated from the fact that the theoretical model did not consider magnetic anisotropy. The combination of the ideal low dimensionality and magnetic isotropy in the calculation might have increased the fluctuations which would stabilize the uud phase, hence yielding larger uud phase area.

Here, we would like to comment on another possible magnetic phase below T_{N3} observed at low fields, which was not theoretically predicted. We speculate that it is a spin reoriented phase with smaller canting angles. The spin reorientation might occur to have smaller canting angles while keeping the magnetic symmetry unchanged. The decrease of χ' below T_{N3} suggests more cancellation of spin vector sums due to smaller canting angles. The phase boundary between PE-FE matches with PM-Y phase, which confirms $Ba_3MnNb_2O_9$ another multiferroic TLAF. This is similar to the multiferroicity of $RbFe(MoO_4)_2$ [7], S-5/2 2D TLAF with an easy plane anisotropy.

Finally, we compare the magnetic phases of $Ba_3MnNb_2O_9$ ($S = 5/2$) with its sister compounds, $Ba_3NiNb_2O_9$ ($S = 1$) and $Ba_3CoNb_2O_9$ ($S = 1/2$). Several differences are noticed: (i) easy-plane magnetic anisotropy for Ni compound and easy-axis for Co and Mn compounds; (ii) 120° spin structure in the ab plane without canting in Ni and Co compound (it is possible that the canting of Co compound is too small to be detected by the NPD in the previous work), while out-of-plane canting for Mn compound; (iii) more stable uud phase at high temperatures in the Mn compound (spreading out at high temperatures) while the opposite is true for the Ni and Co compounds. This difference is consistent with the theories that the quantum fluctuations become more effective at low temperature to stabilize the uud phase for small-spin compounds; (iv) ferroelectricity survives in the collinear spin states in the Ni and Co compound while not in the Mn

compound. Whether the difference is related to either classical or quantum spins can be a subject for future studies.

V. CONCLUSIONS

In conclusion, our detailed studies on $Ba_3MnNb_2O_9$ show that it is a quasi 2D spin-5/2 TLAF with weak easy-axis anisotropy. With increasing magnetic field, successive magnetic phase transitions are observed. The overall behaviors of the magnetic phase diagram are consistent with the theoretical prediction of a Heisenberg TLAF. Moreover, multiferroicity is observed in its low field phase with nonzero spin chirality. Therefore, $Ba_3MnNb_2O_9$ provides another unique example of TLAFs with classical spins showing successive magnetic phase transitions and multiferroicity.

[1] P. W. Anderson, Mater. Res. Bull. **8**, 153 (1973).

[2] A. P. Ramirez, Annu. Rev. Mater. Sci. **24**, 453 (1994).

[3] M. F. Collins and O. A. Petrenko, Can. J. Phys. **75**, 605 (1997).

[4] L. Balents, Nature (London) **464**, 199 (2010).

[5] J. Villian, R. Bidaux, J. P. Carton, and R. J. Conte, J. Phys. (Paris) **41**, 1263 (1980).

[6] A. I. Smirnov, H. Yashiro, S. Kimura, M. Hagiwara, Y. Narumi, K. Kindo, A. Kikkawa, K. Katsumata, A. Ya. Shapiro, and L. N. Demianets, Phys. Rev. B **75**, 134412 (2007).

[7] L. E. Svistov, A. I. Smirnov, L. A. Prozorova, O. A. Petrenko, A. Micheler, N. Büttgen, A. Ya. Shapiro, and L. N. Demianets, Phys. Rev. B **74**, 024412 (2006).

[8] R. Ishii, S. Tanaka, K. Onuma, Y. Nambu, M. Tokunaga, T. Sakakibara, N. Kawashima, Y. Maeno, C. Broholm, D. P. Gautreaux, J. Y. Chan, and S. Nakatsuji, Europhys. Lett. **94**, 17001 (2011).

[9] M. Kenzelmann, G. Lawes, A. B. Harris, G. Gasparovic, C. Broholm, A. P. Ramirez, G. A. Jorge, M. Jaime, S. Park, Q. Huang, A. Ya. Shapiro, and L. A. Demianets, Phys. Rev. Lett. **98**, 267205 (2007).

[10] J. S. White, Ch. Niedermayer, G. Gasparovic, C. Broholm, J. M. S. Park, A. Ya. Shapiro, L. A. Demianets, and M. Kenzelmann, Phys. Rev. B **88**, 060409(R) (2013).

[11] Alexander J. Hearmon, Federica Fabrizi, Laurent C. Chapon, R. D. Johnson, Dharmalingam Prabhakaran, Sergey V. Streltsov, P. J. Brown, and Paolo G. Radaelli, Phys. Rev. Lett. **108**, 237201 (2012).

[12] S. Seki, Y. Onose, and Y. Tokura, Phys. Rev. Lett. **101**, 067204 (2008).

[13] K. Kimura, H. Nakamura, K. Ohgushi, and T. Kimura, Phys. Rev. B **78**, 140401(R) (2008).

[14] J. Hwang, E. S. Choi, F. Ye, C. R. Dela Cruz, Y. Xin, H. D. Zhou, and P. Schlottmann, Phys. Rev. Lett. **109**, 257205 (2012).

[15] M. Lee, J. Hwang, E. S. Choi, J. Ma, C. R. Dela Cruz, M. Zhu, X. Ke, Z. L. Dun, and H. D. Zhou, Phys. Rev. B **89**, 104420 (2014).

[16] T. Kimura, T. Goto, H. Shintani, K. Ishizaka, T. Arima, and Y. Tokura, Nature (London) **426**, 55 (2003).

[17] N. A. Spaldin and M. Fiebig, Science **309**, 391 (2005).

[18] M. Fiebig, J. Phys. D: Appl. Phys. **38**, R123 (2005).

[19] Y. Tokura, Science **312**, 1481 (2006).

[20] S.-W. Cheong and M. Mostovoy, Nat. Mater. **6**, 13 (2007).

[21] K. F. Wang, J.-M. Liu, and Z. F. Ren, Adv. Phys. **58**, 321 (2009).

[22] C. Wang, G.-C. Guo, and L. He, Phys. Rev. Lett. **99**, 177202 (2007).

[23] C. Wang, G.-C. Guo, and L. He, Phys. Rev. B **77**, 134113 (2008).

[24] Y. J. Choi, H. T. Yi, S. Lee, Q. Huang, V. Kiryukhin, and S.-W. Cheong, Phys. Rev. Lett. **100**, 047601 (2008).

[25] H. Katsura, N. Nagaosa, and A. V. Balatsky, Phys. Rev. Lett. **95**, 057205 (2005).

[26] I. A. Sergienko and E. Dagotto, Phys. Rev. B **73**, 094434 (2006).

[27] J. Rodriguez-Carvajal, Physica B **192**, 55 (1993).

[28] G. A. Parks and S. Akhtar, Am. Mineral. **53**, 406 (1968).

[29] Z. Tian, Q. Guo, Z. Ouyang, G. Du, W. Tong, J. Wang, and S. Yuan, Solid State Commun. **191**, 66 (2014).

[30] Y. Shirata, H. Tanaka, A. Matsuo, and K. Kindo, Phys. Rev. Lett. **108**, 057205 (2012).

[31] Y. Shirata, H. Tanaka, T. Ono, A. Matsuo, K. Kindo, and Hiroki Nakano, J. Phys. Soc. Jpn. **80**, 093702 (2011).

[32] H. Kawamura and S. Miyashita, J. Phys. Soc. Jpn. **54**, 4530 (1985).

[33] L. Seabra, T. Momoi, P. Sindzingre, and N. Shannon, Phys. Rev. B **84**, 214418 (2011).

[34] G. Kresse and J. Hafner, Phys. Rev. B **47**, 558 (1993).

[35] G. Kresse and J. Furthmüller, Phys. Rev. B **54**, 11169 (1996).

[36] Y. Liu, R. L. Withers, A. P. Whichello, L. Norén, V. Ting, F. Brink, and J. D. F. Gerald, J. Solid. State Chem. **178**, 3389 (2005).

[37] P. E. Blöchl, Phys. Rev. B **50**, 17953 (1994).

[38] G. Kresse and D. Joubert, Phys. Rev. B **59**, 1758 (1999).

[39] J. P. Perdew, K. Burke, and M. Ernzerhof, Phys. Rev. Lett. **77**, 3865 (1996).

[40] S. L. Dudarev, G. A. Botton, S. Y. Savrasov, C. J. Humphreys, and A. P. Sutton, Phys. Rev. B **57**, 1505 (1998).

[41] H. Kitazawa, H. Suzuki, H. Abe, J. Tang, and G. Kido, Physica B: Cond. Mat. **259-261**, 890 (1999).

[42] G. Giovannetti and J. van den Brink, Phys. Rev. Lett. **100**, 227603 (2008).

[43] D. H. Lee, J. D. Joannopoulos, J. W. Negele, and D. P. Landau, Phys. Rev. B **33**, 450 (1986).